Imaging short-period seismic radiation from the 27 February 2010 Chile (M_W 8.8) earthquake by back-projection of *P*, *PP*, and *PKIKP* waves

Keith D. Koper,[1] Alexander R. Hutko,[2] Thorne Lay,[3] and Oner Sufri[1]

Received 7 June 2011; revised 18 October 2011; accepted 19 December 2011; published 18 February 2012.

[1] Teleseismic short-period (0.5–5 s) *P* waves from the 27 February 2010 Chile earthquake (M_w 8.8) are back projected to the source region to image locations of coherent short-period seismic wave radiation. Several receiver array configurations are analyzed using different *P* wave arrivals, including networks of stations in North America (*P*), Japan (*PKIKP*), and Europe (*PP*), as well as a global configuration of stations with a broad azimuthal distribution and longer-period *P* waves (5–20 s). Coherent bursts of short-period radiation from the source are concentrated below the Chilean coastline, along the downdip portion of the megathrust. The short-period source region expands bilaterally, with significant irregularity in the radiation. Comparison with finite fault slip models inverted from longer-period seismic waves indicates that the regions of large slip on the megathrust are located updip of the regions of short-period radiation, a manifestation of frequency-dependent seismic radiation, similar to observations for the great 2011 Tohoku earthquake (M_w 9.0). Back projection of synthetic *P* waves generated from the finite fault models demonstrates that if the short-period energy had radiated with the same space-time distribution as the long-period energy, back-projection analysis would image it in the correct location, updip. We conclude that back-projection imaging of short-period signals provides a distinct view of the seismic source that is missed by studies based only on long-period seismic waves, geodetic data, and/or tsunami observations.

Citation: Koper, K. D., A. R. Hutko, T. Lay, and O. Sufri (2012), Imaging short-period seismic radiation from the 27 February 2010 Chile (M_W 8.8) earthquake by back-projection of *P*, *PP*, and *PKIKP* waves, *J. Geophys. Res.*, *117*, B02308, doi:10.1029/2011JB008576.

1. Introduction

[2] The M_w 8.8 earthquake that struck Chile (36.122°S, 72.898°W, U.S. Geological Survey (USGS) Preliminary Determinations of Epicenters weekly listing (PDE-W)) on 27 February 2010 was the sixth largest earthquake to occur in modern times. Extensive high-quality geophysical observations have been used to study details of the rupture process. Seismic data analyses include back projection of teleseismic short-period (~0.5–5.0 s) body waves (*P* and *PKIKP*) to track the evolution of the rupture front [e.g., *Lay et al.*, 2010; *Kiser and Ishii*, 2011]; midperiod (~5–500 s) *P*, *SH*, and Rayleigh wave inversions for finite fault models of the space-time moment or slip distribution [e.g., *Delouis et al.*, 2010; *Hayes et al.*, 2010; *Lay et al.*, 2010]; and normal mode (periods of ~500–3200 s) amplitude modeling to detect the presence of any slow component to the rupture [*Okal et al.*, 2010; *Tanimoto and Ji*, 2010]. Geodetic observations in the form of GPS, INSAR, and coastal uplift measurements have provided further important constraints on the time-integrated slip during the earthquake [e.g., *Delouis et al.*, 2010; *Farías et al.*, 2010; *Tong et al.*, 2010; *Lorito et al.*, 2011; *Pollitz et al.*, 2011; *Vigny et al.*, 2011], as have tsunami observations from tide gauges and ocean bottom pressure gauges [*Satake and Fujii*, 2010; *Yamazaki and Cheung*, 2011].

[3] There is now general agreement that the 2010 Chile earthquake was a bilateral rupture that spanned ~450–550 km along strike of the megathrust boundary between the Nazca and South American plates, with maximum slip of ~20 m, seismic moment of ~2.0×10^{22} Nm (M_w 8.8), and faulting duration of 120–140 s. However, many details of the rupture process are still being debated as efforts continue to reconcile the diverse geophysical observations. Early aftershocks extended from ~33.5°S to ~38°S, roughly bounded to the south by the rupture zone of the 22 May 1960 (M_w 9.5) earthquake and to the north by the rupture zone of the 3 March 1985 (M_w 8.2) earthquake [*Comte et al.*, 1986], but the fault slip was not uniformly distributed over the aftershock zone. Instead, strong slip was concentrated in two subregions, a patch with very large slip centered near 35°S, about 50–150 km north of the epicenter,

[1]Department of Geology and Geophysics, University of Utah, Salt Lake City, Utah, USA.
[2]Data Management Center, Incorporated Research Institutions for Seismology, Seattle, Washington, USA.
[3]Department of Earth and Planetary Sciences, University of California, Santa Cruz, California, USA.

0148-0227/12/2011JB008576

and a less well defined patch with lower slip located a somewhat smaller distance to the southwest. Various models for the rupture process indicate slightly different locations and relative strengths for the two strong-slip regions, but all models indicate little or modest slip in the epicentral region. This prompted the suggestion that significant seismic hazard remains near the epicenter, a region that apparently last ruptured in the 1835 earthquake documented by Charles Darwin [*Lorito et al.*, 2011].

[4] In this paper, we present an analysis of the 2010 Chile earthquake rupture process as imaged by back projection of short-period, teleseismic *P* waves. Imaging short-period radiation from large earthquakes has the potential to constrain the rupture velocity and to locate subregions of rapid particle dislocation with better precision than achievable with finite fault inversions, which are limited to modeling seismic energy with periods longer than ~5 s. The primary challenge is that imaging methods have intrinsic, sometimes subtle, artifacts and typically can only be applied to relatively narrow spectral bands, providing an incomplete representation of the faulting process. Back projection, or reverse time migration, of teleseismic short-period wavefields for large earthquakes is a relatively recent approach, popularized by successful application to the M_w 9.2 Sumatra earthquake of 26 December 2004 [*Ishii et al.*, 2005; *Krüger and Ohrnberger*, 2005]. Few of the subsequent studies have evaluated the resolution and limitations of back-projection methods for very large earthquakes, and caution is needed when interpreting back-projection images because of the artifacts inherent to the method and the fact that some features in the images can vary significantly when the frequency band, array geometry, or a tuning parameter is altered, complicating their interpretation.

[5] Our goal here is to explore the robust features of the teleseismic short-period seismic wave radiation for the great 2010 Chile earthquake resolvable by back-projection analyses of the available teleseismic data. This paper has two novel aspects relative to our initial back-projection analysis of the 2010 Chile earthquake [*Lay et al.*, 2010]. First is that we present results from four additional array configurations: 604 *P* waves recorded in North America, 67 *PKIKP* waves recorded in Japan (F-net), 55 *PP* waves recorded in Eurasia, and 43 *P* waves from a global distribution of stations. We quantify the image resolution provided by each configuration by calculating the corresponding array response functions over relevant frequency bands, discussing the strengths and limitations of various geometries and passbands. The second novel aspect is that we back project synthetic seismograms calculated for a suite of finite fault models. Comparison of the spatial distribution of back-projected beam power with the known input slip distributions provides an evaluation of the sensitivity of the back-projection method and gives insight into any bias in the resulting images created by limited bandwidth, variations in Green's functions, and finite fault wavefield interference effects. It also provides an opportunity to compare short-period data source radiation images with slip distributions from longer-period waves as seen through the same processing lens. This enables us to establish important frequency-dependent attributes of the great Chile earthquake rupture.

[6] While coherent bursts of short-period radiation anywhere on the fault during the rupture process can be imaged, it is likely that the most coherent short-period radiation will come from the rupture front approaching the observing network. The propagating crack tip is expected to emit short-period energy and forward directivity will enhance the signal in the direction of rupture propagation. Energy from a propagating crack tip moving away from the observing network will likely be less coherent as it will have interference from the larger moment release patches that rupture later in time, but closer to the network. The degree to which images of loci of short-period radiation correspond to total slip variations or subfault seismic moment is highly dependent upon the combined effects of rupture expansion rate, particle dislocation velocity, and total slip, all of which likely vary substantially over a great earthquake rupture area. There is thus no a priori reason to anticipate perfect correspondence between short-period radiation and total slip distribution for a large earthquake. A fundamental question that we address for the 2010 Chile earthquake is, How does the imaged short-period radiation relate to the total rupture process?

2. Back-Projection Methodology

[7] Our back-projection procedure closely follows that described by *Xu et al.* [2009]. For a given distribution of receivers, the seismograms are aligned on a reference (typically initial) phase using a multichannel cross-correlation algorithm (MCCC) [*VanDecar and Crosson*, 1990]. This generates a suite of static time corrections that account for the image blurring created by 3-D variations in Earth structure along the general path between the source region and the receivers. The corrections are defined relative to travel time predictions calculated through AK135 [*Kennett et al.*, 1995] for the final USGS National Earthquake Information Center (NEIC) location (epicenter of 36.122°S and 72.898°W, depth of 23 km, origin time of 06:34:11 GMT).

[8] The seismograms are then amplitude normalized and time shifted for propagation through the reference model AK135 [*Kennett et al.*, 1995] (plus the MCCC-derived static corrections) to a 3-D grid of potential source radiation locations evenly distributed in space (latitude and longitude) and time. For each assumed grid point a beam is formed by stacking the move out shifted seismograms, and the power is calculated from a short, tapered window centered on each target image time. Space-time points that show high relative beam power are inferred to be intervals of coherent short-period radiation from the rupture surface.

[9] For all results presented here the same basic geometry was used to discretize the source region. Each cell was 0.1° by 0.1° and the grid extended in latitude from −32° to −39°, and in longitude from −67.5° to −76.5°. The depth was held fixed at a nominal value of 23 km since there is virtually no relative depth resolution over a shallow-dipping fault for teleseismic arrival times. Trial radiation times over the entire grid began 20 s before the nominal origin time (06:34:11 GMT) and were shifted in steps of 1 s for a total time interval of 220 s. The length of the sliding window used to calculate beam power was 10 s and a Bartlett taper was applied. We experimented with variations of these parameters and found insignificant changes to the resulting images.

[10] The type of stacking used to construct the beams has a major effect on the results. We compared two styles of beam

formation, linear delay-and-sum stacking versus nonlinear Nth-root stacking [*Kanasewich et al.*, 1973; *Muirhead and Datt*, 1976; *McFadden et al.*, 1986]. We experimented with N = 2, 3, 4 and found that the spatial spread of beam power was much smaller for Nth root stacking than for linear stacking, effectively sharpening the array response function. This advantage cannot be replicated using nonlinear color scales to represent linear beam power because in some cases the image maxima change locations. The differences in images created with cube-root and fourth-root stacking were very small, implying that higher-order roots do not provide further advantage. No matter what stacking procedure is used, there is significant uncertainty in defining actual source dimensions for the coherent energy, as the finite frequencies of the signals will spread stacked energy over space and time.

[11] A final postprocessing step involved averaging the geographical distribution of beam power over a series of time frames. This dampens the "swimming" artifact in which each discrete energy bundle in a back projection appears to propagate across the source region in the direction of the receiver array (peaking at the optimal time/location combination). The swimming is a manifestation of the array response to a space-time point source and could be avoided in theory by using an array that had a more uniform azimuthal distribution; however, in many cases the radiation pattern of the source would lead to variable *P* wave trains at such an array and constructive interference would not be possible. The time averaging yields smoother images of beam power, effectively acting as a simple slowness filter, but there is again a blurring of energy over space that complicates inference of source dimension. The window length used in the averaging was 20 s. Varying this length had some effect on the images, but our choice was suitable for dampening the swimming artifact while still allowing for spatial movement of the beam energy related to actual rupture propagation.

[12] Additional aspects of back projection that are important to keep in mind is that there is no deterministic accounting for Green's functions, so the images are not direct estimates of seismic moment or slip, and absolute amplitudes are strongly influenced by wavefield coherence, which may be reduced for extended source regions. The energy that stacks coherently may involve downgoing signal, upgoing signal (depth phases), or some combination of both, with interference between different phases likely contributing to some "burstiness" of the images that may not reflect true source radiation irregularity. Several of the above complicating attributes of back projection are addressed below.

3. Data Images

3.1. Back Projection of *P* waves Recorded in North America

[13] Our initial back-projection analysis of the 2010 Chile earthquake [*Lay et al.*, 2010] used a sparse array of 49 seismometers located in North America. *P* waves from the selected stations all had high cross-correlation values according to an MCCC analysis of a larger group of regional stations. The stations were also selected to provide quasi-uniform coverage across North America. Here we use a much larger number of stations to evaluate any advantage provided by a higher density of sensors covering essentially the same area. Although signal-to-noise ratio on a particular beam is expected to increase as $\sqrt{N}$ if the noise is uncorrelated, where N is the number of elements, it does not necessarily follow that more elements yield a better array response function because of the complicated trade-offs between the strength, size, and separation of the array response sidelobes.

[14] We augmented our original data set with over 600 vertical component seismograms from North American stations including the Earthscope Transportable Array. The MCCC algorithm was applied to the unfiltered broadband traces, starting 5 s before the theoretical *P* arrival and ending 15 s later. Stations with a correlation coefficient less than 0.85 were removed, leaving 604 traces that were then realigned using MCCC. Each trace was also normalized by its peak amplitude in the MCCC window. Figures 1a and 1b show the aligned seismograms and the corresponding station map.

[15] For comparison with our earlier results we used the same frequency band, defined by a four-pole Butterworth filter with corners at 0.2 and 2.0 Hz. This band was originally selected because coherence drops off quickly above 1–2 Hz while resolution drops off quickly below 0.2 Hz. We performed numerous back projections, with the output from the fourth-root analysis presented in Figures 1c and 1d. Figure 1c shows the maximum beam power as a function of time, while Figure 1d shows the spatial distribution of beam power for six time steps.

[16] Figures 1e–1h we reproduce the results from the sparse North American array using exactly the same processing as for the dense North American geometry. The main difference between this run and that in Figure 2 of *Lay et al.* [2010] is the postprocessing smoothing described earlier. In general, the agreement is very good, with both runs showing significant beam power for about 140 s, with a maximum ~80 s after the origin time. In both cases, this peak energy burst is located in a region about 150–250 km northeast of the epicenter along the Chilean coastline. The major difference between the two network images is the relative amplitude of an earlier peak in beam power near 30 s that corresponds to energy radiated from just downdip of the epicenter. The dense array indicates a beam power near 30 s about 1/2 of the maximum, while the sparse array gives a beam power about 3/4 of the maximum. The sparse array also shows slightly more energy to the south of the epicenter than the dense array, although in both runs the southern feature is subtle, and the dominant impression is of unilateral rupture toward the network, consistent with the notion of preferential sensitivity to forward directivity from the rupture front. Short-period energy from the southwest is likely less coherent for this along-strike configuration since arrivals from equivalent subevents that propagate away from the network would have smaller time separations, causing more interference.

3.2. Back Projection of *PKIKP* Waves From Japan

[17] The second array geometry consists of F-net stations in Japan at distances of 150°–162° for which *PKIKP* is the first arriving phase. We obtained 69 seismograms and used

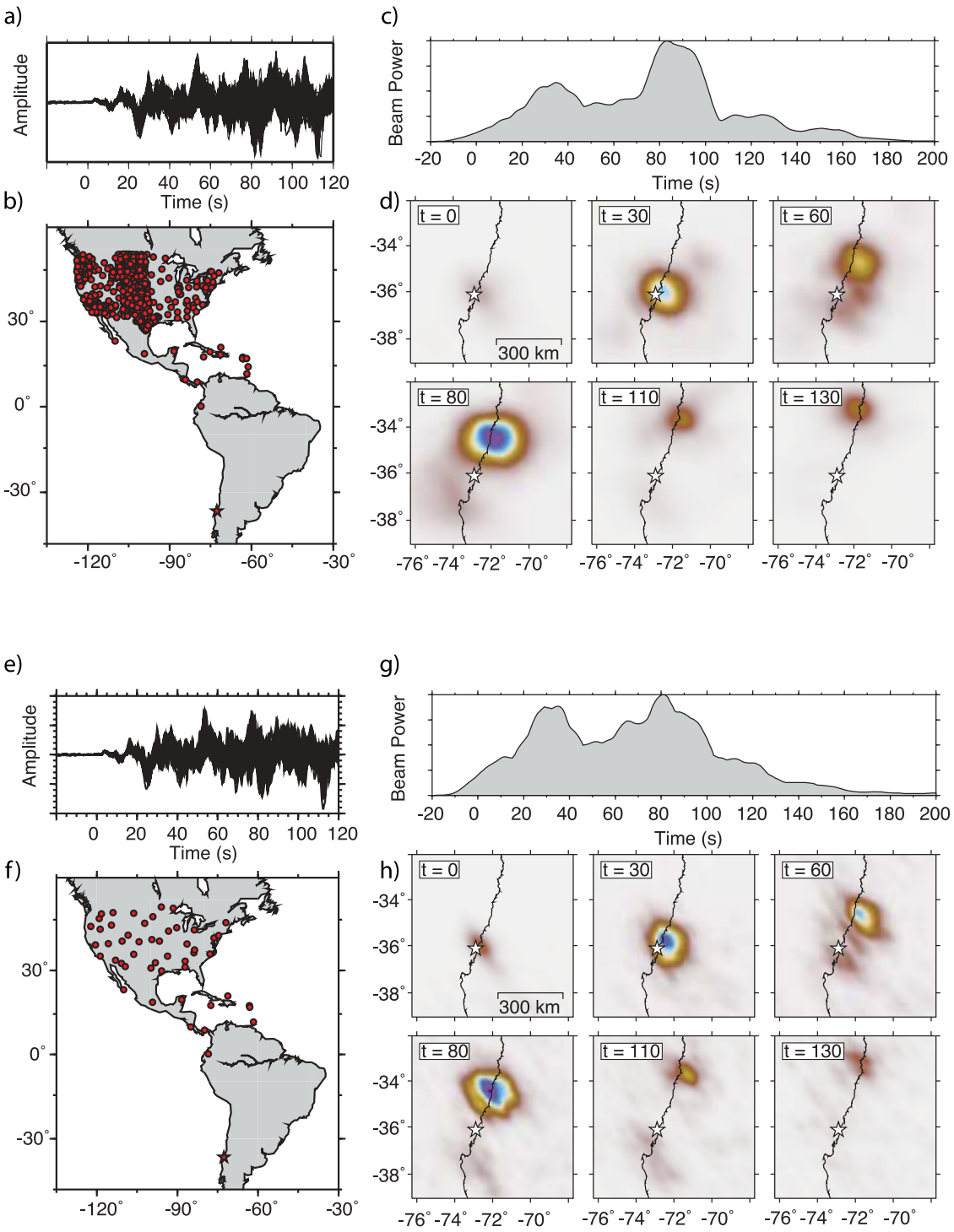

Figure 1. Summary illustration for the back projection of 0.2–2.0 Hz *P* waves recorded across North America by (a–d) a dense array of 604 stations and (e–h) a sparse array of 49 stations. Station locations are indicated by red dots in Figures 1b and 1f, and corresponding aligned *P* waves are shown in Figures 1a and 1e. Normalized beam power as a function of time is shown by the gray curves (Figures 1c and 1g), while snapshots of the rupture are presented for lapse times of 0, 30, 60, 80, 110, and 130 s (Figures 1d and 1h). The beam power color scale is linear and varies from off-white through purple as defined by the globe palette in GMT [*Wessel and Smith*, 1991]. In each geographical panel in Figures 1d and 1h the original U.S. Geological Survey (USGS) epicenter is shown with a white star. Animations from these back projections are included in the auxiliary material.

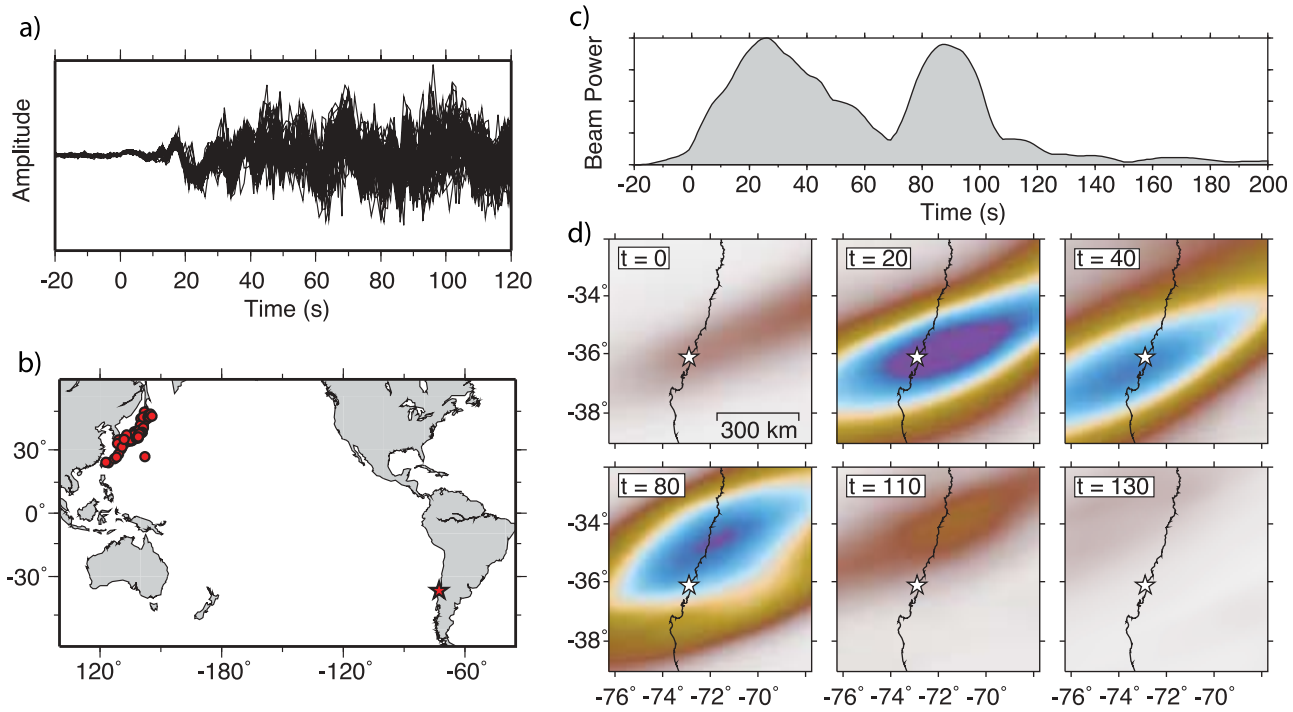

Figure 2. Summary illustration for the back projection of sixty-seven 0.2–1.0 Hz *PKIKP* waves recorded by the F-net array in Japan. The panels are defined as in Figure 1. An animation from this back projection is included in the auxiliary material.

the 67 that had average correlation values higher than 0.76. The MCCC was run as before, on unfiltered traces with windows extending from 5 s before the theoretical arrival time until 10 s after. The resulting traces and station locations are shown in Figures 2a and 2b.

[18] We experimented with several frequency bands for back projecting these *PKIKP* data. Coherence dropped off more quickly with frequency than for the North America *P* waves, and we ultimately selected a band defined by a four-pole Butterworth filter with corners at 0.2 and 1.0 Hz. The results of a fourth-root back projection are presented in the Figures 2c and 2d. The time dependence of the beam power has a fair resemblance to that in Figure 1. In particular, the maximum power is achieved approximately 80–85 s after the origin time, while a second peak with nearly the same amplitude exists at about 25 s.

[19] The spatial positions of the energy peaks are far less certain for the *PKIKP* data than for the direct *P* to North America because of the higher apparent velocities and smaller aperture of the Japan network. This severely limits the lateral resolution of the rupture location, but what resolution is obtained is mainly along the fault strike. It is suggested by the frames shown in Figure 2 that the *PKIKP* back projection supports a bilateral rupture with a coherent burst of energy about 100–200 km northeast of the epicenter. There seems to be little interference caused by later arriving PKP_{AB} energy, most likely because it has lower apparent velocity than *PKIKP* and thus interferes destructively when it is back projected with *PKIKP* travel time move out. One can use different color schemes to enhance apparent localization of short-period radiation, but this is inconsistent with the intrinsic diminished resolution expected for these phases.

3.3. Back Projection of *PP* Waves From Eurasia

[20] A network comprising seismometers located in Europe and Asia at distances of 70°–160° from the source region, with *PP* as the reference phase, was also analyzed. At these distances, *PP* has apparent velocities equivalent to those of *P* waves at distances of 35°–80°, and so offers comparable lateral resolution. Furthermore, these waves leave the source to the northeast and thus sample a distinct portion of the focal sphere with different dominant Green's functions compared to phases observed in North America and Japan, providing a third independent view of the rupture. On the other hand, *PP* waves naturally have lower-frequency content than *P* waves because of the extra travel time spent in the attenuating upper mantle, which reduces resolution, and scattered energy from precursory phases makes the initial alignment of *PP* more difficult.

[21] We originally examined data from 91 seismograph stations across Eurasia. We experimented with different control parameters for aligning the phases via MCCC, and ultimately retained 55 seismograms. These had average correlation coefficients above 0.6 for an MCCC run on unfiltered traces using a window that started 5 s before the expected arrival time and lasted for 15 s. The aligned and normalized traces are presented in Figure 3a, which clearly shows the lower-frequency content of the *PP* waves compared to *P* (Figure 1) and *PKIKP* (Figure 2). We experimented with various frequency bands to test the coherence of the *PP* wave train, and found that a filter with corners of 0.1 and 0.5 Hz provided the best results. Raising the lower corner up to 0.2–0.3 Hz diminishes the coherence enough that robust imaging is not possible. The differences in

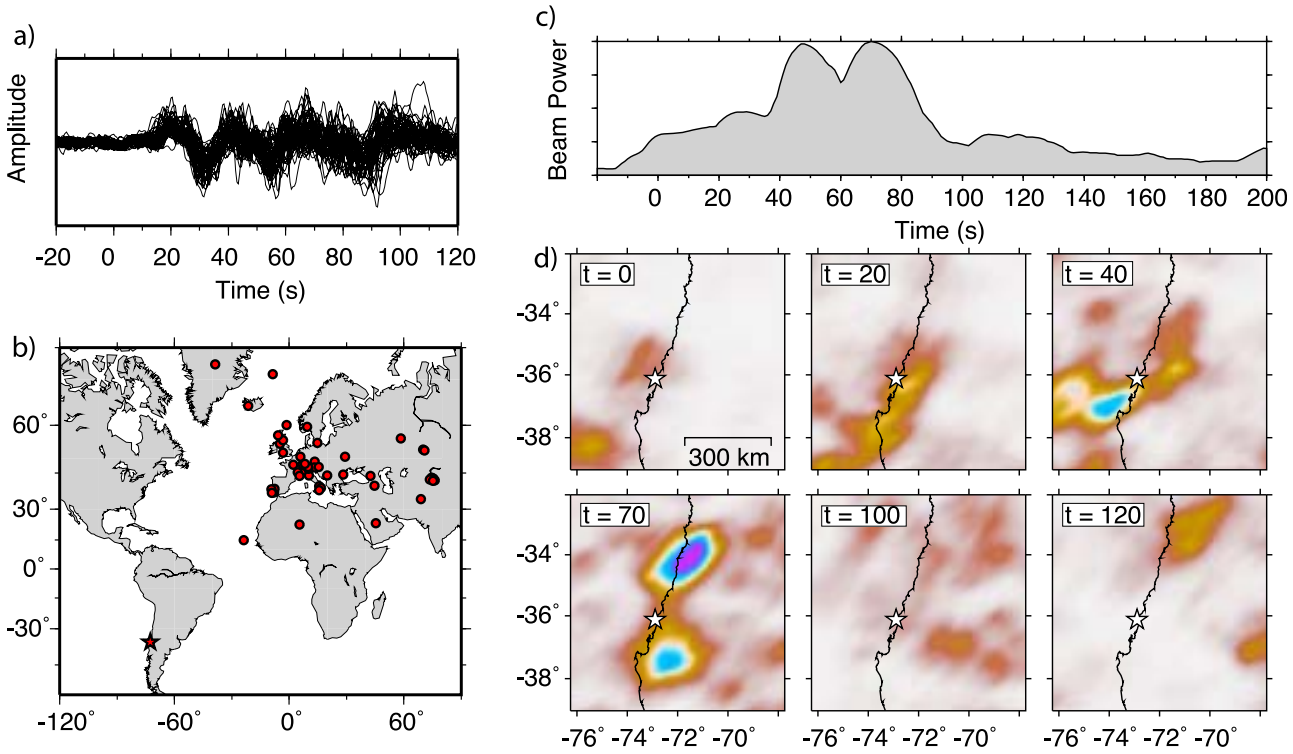

Figure 3. Summary illustration for the back projection of fifty-five 0.1–0.5 Hz *PP* waves recorded across Europe. The panels are defined as in Figure 1. An animation from this back projection is included in the auxiliary material.

passband should be kept in mind when comparing the images with those for other networks.

[22] Results of the *PP* back projection are shown in Figures 3c and 3d, with the same format as in Figures 1 and 2. Some features of this run are similar to those carried out with *P* waves from North America, and *PKIKP* waves from Japan: significant beam power exists for 120–140 s with rupture patches mainly along strike of the plate boundary, and with energy imaged both to the south and the north of epicenter. The dominant feature is again an energy source located near longitude −72°, latitude −34°, however it appears about 10 s earlier than in the other images. The reason for this is unclear but may be related to the lower-frequency content of the waves used for the *PP* back projection, which may modify effects of the depth phase interference, and the fact that alignment of the beginning portion of *PP* is hindered by the presence of coda of earlier arriving phases. Relative short-period source energy imaged to the south is significantly stronger for this configuration than for the other cases.

3.4. Back Projection of *P* Waves From a Sparse Global Configuration

[23] The final array geometry we considered is a globally distributed set of seismometers, all at distances of 30°–90° from the epicentral region, with the direct *P* wave as the reference phase. Because of the wide azimuthal coverage, this array geometry offers the best formal resolution for locating the early features in the rupture in space and time; however, the seismic energy will also be less coherent between stations relative to the regional network geometries because of wide sampling of the azimuthally varying Green's functions. On the basis of MCCC experiments, we ultimately selected 42 seismograms, each having a correlation coefficient larger than 0.6 for the first 10 s of the *P* wave train. For seven of the stations the polarity was inverted prior to the MCCC, as expected by their location in the focal sphere. The aligned seismograms are presented in Figure 4a, and the corresponding station locations are presented directly below.

[24] Owing to the low coherence of the *P* waves we used a lower-frequency band defined by a four-pole Butterworth filter with corners at 0.05–0.20 Hz. This is in the frequency band where deterministic modeling of waveforms performs well, and there is not a clear advantage to back-projection imaging, other than to perhaps resolve the centroid of early radiation and any coherent short-duration subevents later in the rupture. Many sources do appear to involve superimposed discrete subevents of similar character, and in that case the event relative timing and spatial position may be recovered by back projection of azimuthally distributed lower-frequency data. Such an image is expected to differ from what may be sensed for short-period signals recorded by a localized array with a smaller footprint on the focal sphere.

[25] Results from the fourth-root back-projection run are shown in Figures 4c and 4d. Although beam power spreads significantly along strike in a bilateral sense, the major release imaged occurs within the first few tens of seconds, just downdip and to the south of the epicenter. This is in contrast to results from the three other configurations in which the maximum beam power occurred to the north,

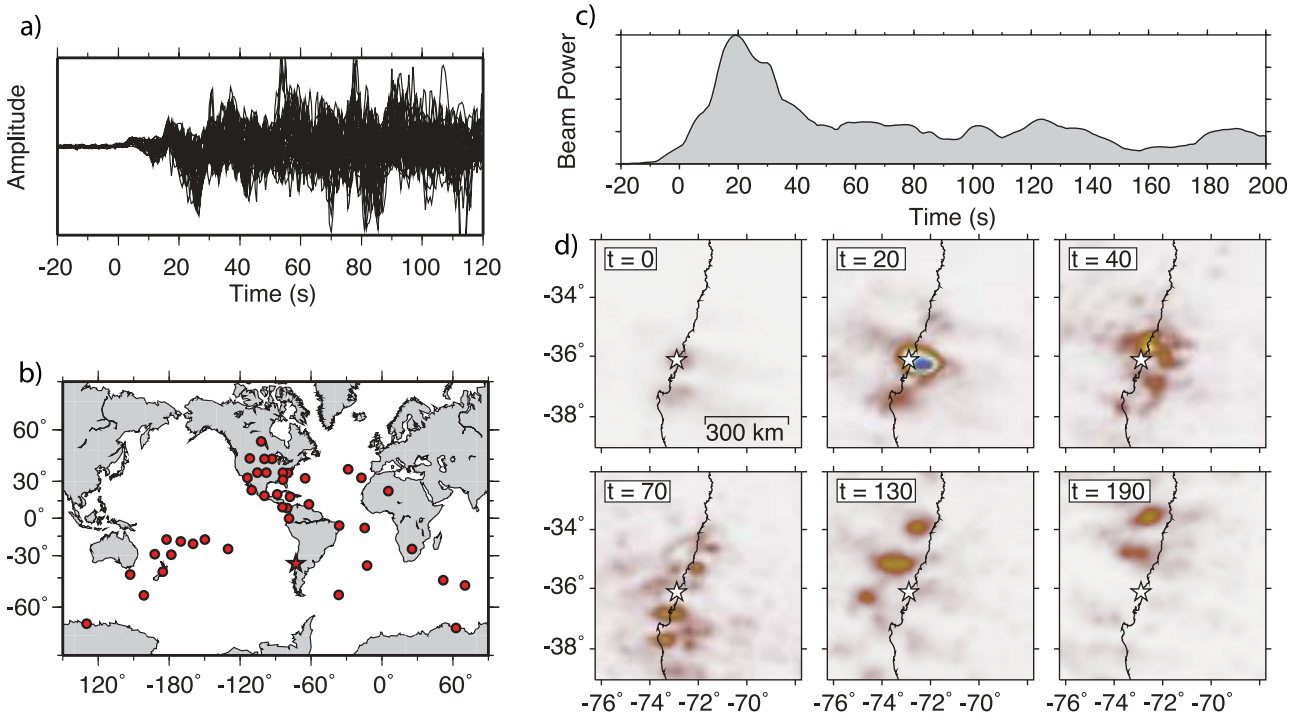

Figure 4. Summary illustration for the back projection of forty-three 0.02–0.2 Hz *P* waves recorded across the globe. The panels are defined as in Figure 1. An animation from this back projection is included in the auxiliary material.

75–85 s after the origin time. There are secondary peaks of beam energy to the north and south, suggesting that at some stages of the bilateral fault expansion coherent 5–20 s energy came from localized regions, but the lack of wavefield coherence for this configuration argues against detailed interpretation of these features, even though the images appear to have some aspects in common with those from regional networks.

[26] The difference between back-projection images from the global configuration and those from the four previously considered configurations is highlighted in Figure 5, in which we present maps of time-integrated beam power. In addition to the lack of coherence of the *P* wave trains recorded globally, Figure 5 hints at the varying levels of resolution provided by the array geometries, especially the poor sensitivity of *PKIKP* waves recorded at F-net. In sections 4 and 5 we quantify the capability of each array to image the space-time location of short-period radiation from the source region.

4. Comparison of Array Response Functions

[27] The spatial resolution provided by the various array geometries can by compared by calculating their array response function (ARF). Traditionally, this function shows the spread in wave number space of beam power associated with a single plane wave arriving across a small- or medium-aperture array [*Rost and Thomas*, 2002]. Alternatively, the ARF can be viewed in slowness space for a specific frequency or range of frequencies. Here we use a modified ARF that is appropriate for non-plane wave propagation across a wide aperture array [*Xu et al.*, 2009]. It presents the spread in beam power as a function of spatial coordinates, and so depends weakly on the assumed near source velocity model (AK135 in this case).

[28] In Figure 6 we show the ARF for our five array configurations, each at three distinct frequencies. For an ideal array the ARF would be a single spike colocated with the epicenter. The spread of the main lobe, as well as the existence of sidelobes, is created by the finite and discrete nature of the array. The fundamental pattern scales linearly as a function of frequency, and as frequency decreases there is a corresponding decrease in resolution. The pattern of sidelobes and the particular shape of the main lobe also change as the array geometry changes.

[29] The effect of station density on back-projection resolution is best illustrated by comparing the ARFs of the sparse and dense North American arrays. The sparse array has a smaller main lobe and lacks the two large secondary sidelobes; however, the main lobe for the sparse array is less symmetrical and has larger sidelobes at further distance from the main lobe than the dense array. These effects are manifested in the back projections of the data for these two configurations shown in Figure 1. The results are similar overall; however, the beam power for the dense array generally looks more symmetrical yet broader, and there are fewer secondary artifacts away from the main concentration of beam power.

[30] The weaknesses of the other configurations are also evident in Figure 6. The Japan *PKIKP* network configuration has a wide main lobe relative to the North American configurations, providing about an order of magnitude poorer resolution at equivalent frequencies. The main contribution of this geometry is in having an azimuthal

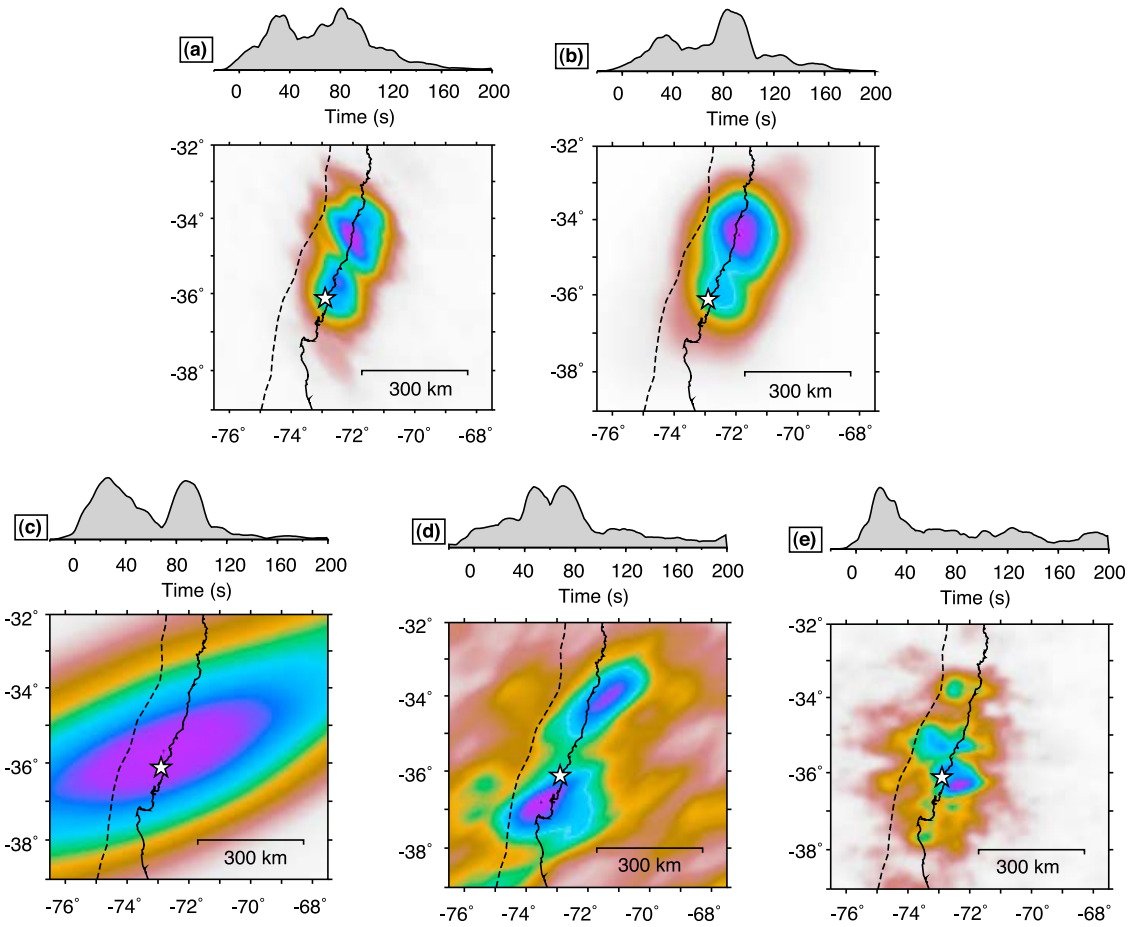

Figure 5. Time-averaged beam power for the five back-projection simulations presented in Figures 1–4. We show results for (a) the sparse North America *P* configuration, (b) the dense North America *P* configuration, (c) the Japan *PKIKP* configuration, (d) the Europe-Asia *PP* configuration, and (e) the global *P* configuration.

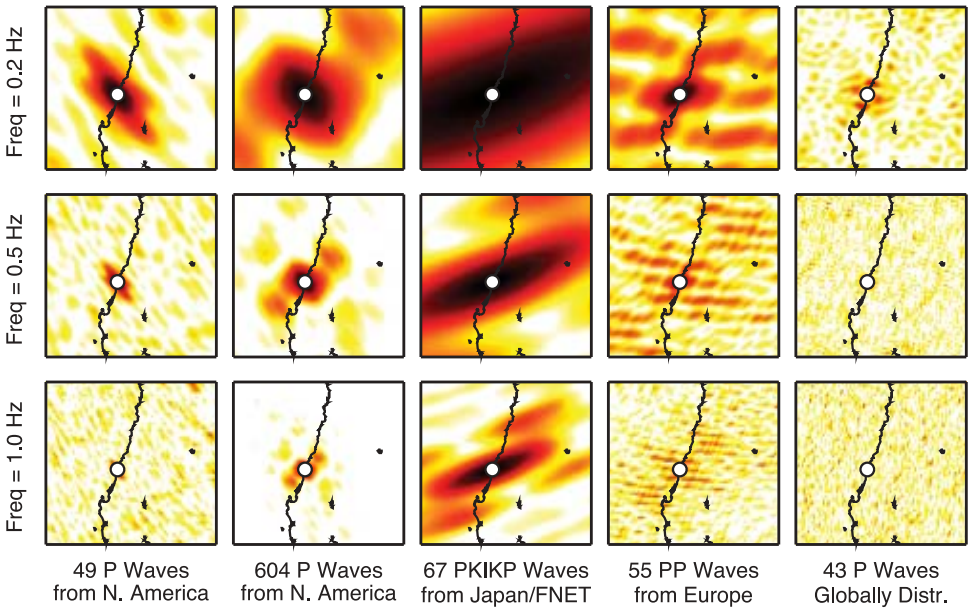

Figure 6. Array response functions for the five station geometries considered in this work. Frequency varies from (top) 0.2 Hz to (middle) 0.5 Hz to (bottom) 1.0 Hz. The color scale is in decibels, with yellow indicating 1% of the maximum. The original USGS epicenter is shown with a white circle in each panel.

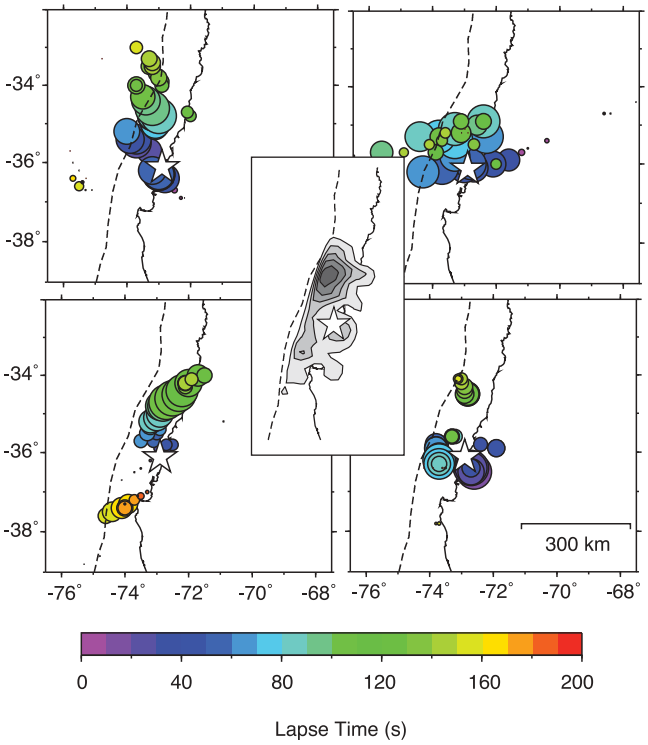

Figure 7. Results of back projecting synthetic seismograms created from our preferred finite fault model. The slip model is shown in the center panel, while back-projection results are shown for the following station geometries: *P* wave in North America, *PKIKP* waves in Japan, *PP* waves in Eurasia, and a global distribution of *P* waves.

orientation that is nearly perpendicular to the North American configurations. Therefore, the swimming artifacts apparent in the animations in the auxiliary material migrate in a perpendicular manner, and along trench-strike features of the rupture are intrinsically better isolated.[1] For instance, the large northern energy source appears clearly in both geometries at about the same time and space in Figures 1 and 2, but energy from the southern portion of the rupture plane is more evident in Figure 2 as Japan has a more favorable geometry for sensing it. The Eurasian *PP* configuration offers main lobe resolution nearly equivalent to that of the sparse North American configuration because of the similar apparent velocities and large network aperture involved, but has much stronger sidelobes at large distances from the main lobe along the average great circle azimuth to the network.

[31] The sparse, global configuration of *P* waves formally offers the best resolution for perfectly coherent signals as evidenced by its small, symmetric main lobe for the 0.2 Hz ARF (Figure 6). Because relatively few stations are included there is significant fuzziness from secondary lobe energy, but this is of the same order as for the sparse North American geometry. This apparent resolution is expected because it is well known that in earthquake location, precision is improved as azimuthal coverage increases. However, this calculation illustrates the weakness of using an ARF alone to judge the likely performance of array configuration in back projection because it assumes perfect coherence among the wave trains recorded at the various elements, which is clearly not the case for widely distributed recordings even for relatively long-period signals from a great earthquake. Effects such as azimuthally dependent depth phase excitation and pulse broadening are not accounted for in the ARF, and these will tend to corrupt back-projection images for a configuration that samples a wide portion of the focal sphere. Rather than trying more sophisticated assumptions about predicted signal decorrelation, we process synthetic waveforms to evaluate effects of Green's function variations for the different network geometries and frequency bands.

5. Back Projection of Synthetic Seismograms From Finite Fault Models

[32] To evaluate how the incoherence of waveforms associated with quasi-realistic Green's function variations can degrade the corresponding data back-projection images, we back project synthetic waves computed for a space-time finite fault slip model (FFM) of the 2010 Chile event. The synthetics explicitly incorporate propagation effects such as geometrical spreading, azimuthal variation in amplitudes and polarities of the direct phase and associated depth phases for a simple layered source structure and variable rake on the fault, and depth variation over the dipping rupture plane along with subfault rupture variations and kinematic expansion of the rupture area. Actual data are expected to have even more variations because of true 3-D Green's functions, variable attenuation, etc., so the results for synthetics can be interpreted as a minimum level of expected back-projection image degradation. These experiments also give insight into how slip and slip variations are manifested in back-projection images of beam power.

[33] The slip map of the initial finite fault slip model used to generate the synthetics is shown in the center panel of Figure 7. This model was determined by inversion of 38 teleseismic *P* and *SH* waves assuming a rupture velocity of 2.0 km/s on a fault plane with constant strike of 18° and dip of 18°. The model parameterization is very similar to that in *Lay et al.* [2010], with 20 km × 20 km subfaults in a grid with 23 cells along strike and 8 along dip. Each subfault has a source time function parameterized by 6 triangle subevents with 3 s risetime and 3 s fall time shifted by 3 s overlaps. Each subevent moment and rake value can vary, with the total subfault rupture duration being 21 s. The model provides excellent waveform variance reduction for signal periods longer than 5 s, and is representative of other slip models determined from teleseismic signals for this event in that the major slip occurs significantly offshore and updip of the back-projected short-period energy. Synthetic seismograms from this model were computed for each station in four array geometries (sparse North American *P*, F-net *PKP*, EU *PP*, and global *P*). The full complexity of the subevent/subfault finite fault rupture was included in the synthetics using dislocation theory as in the data inversions. This is not expected to predict very realistic short-period energy below the 0.5 s sampling used in the inversion, but what short-period energy is produced is compatible with the

[1] Auxiliary materials are available in the HTML. doi:10.1029/2011JB008576.

slip model. The displacement synthetic seismograms were converted to velocity, resampled to 0.025 s, and aligned and normalized via MCCC, just as the actual data were. The same Butterworth filters applied to the data were applied to the synthetics and the same back-projection processing was applied.

[34] The outer panels of Figure 7 show the results of the synthetic back projections using fourth root stacking. Maximum beam power is output every fourth time step (i.e., every 4 s) with circle size directly proportional to beam power, and color indicating the time step. Because of the smearing effect of the array response, each circle should not be considered the location of a discrete source of short-period energy. All four back projections recover energy with dimensions that roughly match the spatial extent of the input slip model, however there is significant variation in the distribution of beam power in space and time. The North American geometry gives the truest match to the slip model with strong beam power in the areas of high-slip located updip and to the north, although it lacks significant beam power south and west of the epicenter. Importantly, there is no downdip bias or smearing in the back-projection results: the major northern slip zone is imaged just to east of the trench, far to the west of where beam power in the data images is located (see Figures 1 and 5).

[35] The European *PP* geometry locates the northern slip zone nearly as well, but energy is smeared slightly toward the coastline. None of the strong slip near the epicenter is visible in the back-projection images; however, the *PP* geometry does recover the strong southern slip, consistent with what is seen in the data images (Figures 3 and 5). The two other array geometries perform worse. The FNET *PKP* configuration shows some northern energy although it is heavily skewed by the array response and gives very poor resolution along dip. Unlike the *PP* geometry, there is no suggestion of energy associated with slip south of the epicenter. The global *P* configuration shows energy concentrated near the epicenter with only a small cluster of sources located to the north. This is also consistent with results from our data back projections for the global configuration (Figures 4 and 5) and confirms that at least for this earthquake the global geometry provides only minimal constraints on the rupture properties, even at relatively long periods. Our general experience is that global array back projections for other events are similar, and only in a few cases are reliable locations of secondary features resolved. The problem is even more severe at shorter periods, but the relatively smooth finite fault models and actual data all have very low coherence over large azimuthal ranges, so resulting back-projection images are not reliable for this large rupture.

[36] Considering that the North America geometry appears more effective than any of the other array configurations in recovering rupture properties of the Chile earthquake, we focus further synthetic experiments on this array. In particular, we examine how well back-projection beam power matches input slip distributions for a suite of finite fault models of varying dimensions. In theory the back-projection imaging of velocity seismograms, as done here, should be most sensitive to changes in slip and not necessarily resolve the slip itself, so significant differences are possible.

[37] Seven finite fault models were constructed by inverting teleseismic *P* and *SH* data with distinct constant rupture velocities ranging from 1.5 to 3.0 km/s in steps of 0.25 km/s. The dip and strike of the fault plane were both fixed at 18° in each case. Subfault source time function parameterizations were the same as described above. The model grid dimensions were scaled in proportion to the rupture velocity for the along-strike dimension, but were held fixed for the dip dimension in order to impose some similarity on the degrees of freedom of the various models. The longer fault dimensions for higher rupture velocities still intrinsically have somewhat more degree of freedom to accommodate directivity and travel time variations, so corresponding inversions tend to give slightly better overall waveform misfit reductions.

[38] Synthetic *P* waves for each of the seven rupture models were computed for all stations in the sparse North America network geometry shown in Figure 1f and band-pass-filtered synthetics were back projected in the same manner as the actual data. Only a couple of stations from this network were used in the inversions for the finite slip models. The frequency passband was 0.2–2.0 Hz, and both linear and fourth root back projections were carried out for each rupture model. The slip models are primarily constrained by signal energy with periods longer than a few seconds, so the synthetic predictions of very short period energy for these models are again not expected to match short-period observations, but should track long-period features for the slip models. Time integrated beam power for three of the models is compared to the corresponding input slip distributions in Figure 8. The time and space location of the northern offshore strong slip patch in the finite fault models is generally well imaged for each rupture velocity model, while the weaker model slip to the south of the epicenter is slightly less well recovered in each case, consistent with the expectation of better imaging of energy in the forward propagating rupture direction where there is larger slip. Even so, the total along-strike extent of the fault zone estimated from the region of significant beam power corresponds quite well to the varying length of the fault zone in the finite fault models.

6. Comparison of Short- and Long-Period Seismic Radiation

[39] Both our earlier finite fault model [*Lay et al.*, 2010] and the current preferred model (Figure 7) place most of the significant slip well offshore of the Chilean coast. This is also true of other finite fault inversions of seismic, geodetic, and tsunami data [e.g., *Lorito et al.*, 2011; *Luttrell et al.*, 2011; *Pollitz et al.*, 2011; *Vigny et al.*, 2011]. Our seismic models tend to place slip somewhat farther offshore than the geodetic models, although they are not very different from those of *Vigny et al.* [2011]. In part this is because we include a layered velocity structure with rigidity decreasing at shallow depth, which enhances updip slip. The geodetic inversions have decreasing resolution of slip further from shore, so the precise location of the updip distribution of slip is not strongly constrained, as pointed out by *Vigny et al.* [2011]. The rupture velocities that best align the regions of large fault slip along strike with those inferred from geodetic inversions and our own tsunami modeling are values of

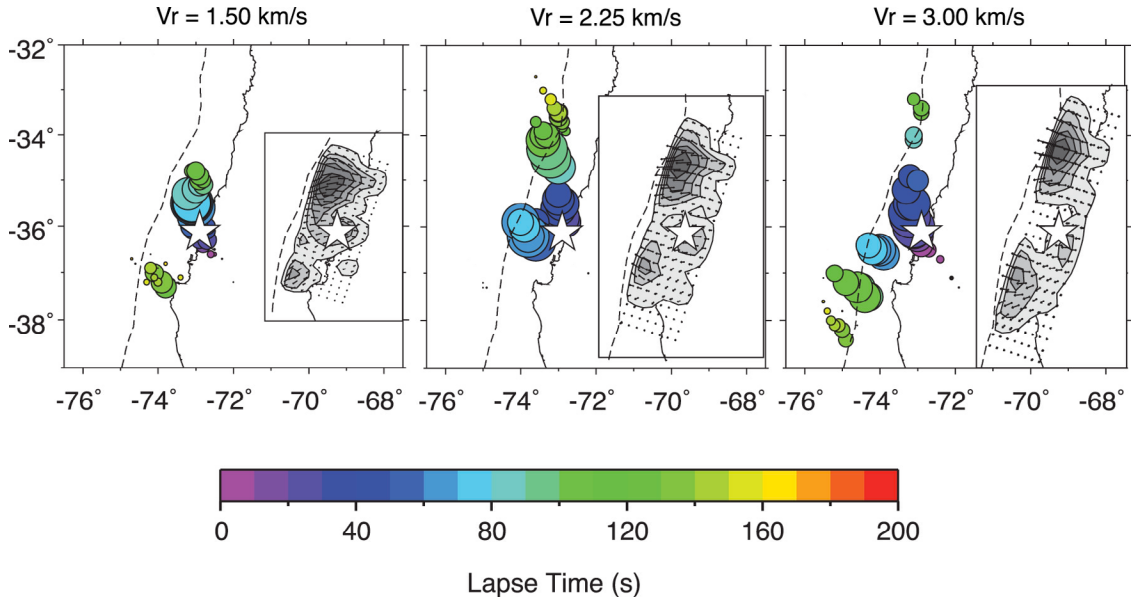

Figure 8. Comparison of back-projection energy from synthetic *P* wave trains and the slip models used to create the synthetics for the sparse North American configuration of seismometers. The three finite fault models were developed by fitting teleseismic body wave data as described in the text, with assumed rupture velocities of 1.5, 2.25, and 3.0 km/s. The time-integrated slip in each model is shown in the insets with gray shaded contours, and the back-projection energy is indicated by circles, with the size proportional to power and the color indicating the time. The white stars represent the original USGS epicenter.

1.75–2.0 km/s, which is lower than the 2.5 km/s used by *Lay et al.* [2010]. That higher velocity was originally imposed on the basis of averaging along-strike rupture velocity estimated from back projections (2.5–3.5 km/s) and from short-arc Rayleigh wave (R1) directivity (2.0–2.25 km/s). Given the excellent resolution of slip location along strike provided by geodetic constraints, we infer that there is a significant "disconnect" between the apparent rupture velocity from back-projection imaging and suitable expansion velocity of the rupture area with large slip. There is also a discrepancy between location of the main fault slip offshore from all long-period seismic, tsunami, and geodetic analyses, and the back-projection imaging of short-period radiation sources right beneath or landward of the Chilean coastline [*Lay et al.*, 2010*; Kiser and Ishii*, 2011].

[40] Given the demonstration that short-period energy from the rather smooth finite-fault model should image offshore where the large slip is located (Figure 8), the downdip concentration of short-period radiation in the actual data migrations landward of the large slip regions of the fault (Figures 1 and 3) [*Kiser and Ishii*, 2011], and the apparent difference in fault area expansion rate indicated by the short-period imaging and the long-period finite fault inversions, it is clear that one cannot infer detailed attributes of the slip process for the Chilean event from network back projections of short-period signals. While there is clearly source information in the back projections, it appears to correspond to high rupture velocity radiation in space-time areas that do not necessarily have large slip during the main faulting.

[41] Figure 9 explores this issue further, comparing the slip distribution from our updated and preferred rupture model with a rupture velocity of 2 km/s and adjusted grid model parameters, to the back projection of actual filtered data (0.2–2.0 Hz) for the sparse North American network configuration with fourth-root stacking. This slip model compares very well with inversions of geodetic observations and tsunami signals, and we think it is a good representation of the primary resolved slip features of the 2010 Chile earthquake. The back projection is presented as both time-integrated beam sum at each grid node and with beam maxima plotted at every fourth time step. There is a clear, spatial offset that implies a frequency dependence to the seismic radiation; lower-frequency energy used to construct the slip models appears offshore, and short-period data used to construct the back-projection images appears downdip on the megathrust, near or eastward of the coastline, and significantly to the north of major slip. We highlight this point in Figure 10, by zooming in on the northern portion of the rupture, and comparing the locations of the largest slip zones from various seismic and geodetic finite-fault inversions (all concentrated near 35°N) with the peak back-projection power for the dense North American image, as well as the back-projection results of *Kiser and Ishii* [2011]. The along-strike and along-dip separation of the back-projection images relative to the slip models is clear.

[42] We also looked for frequency dependence in the rupture properties of the great 2010 Chile earthquake in the back-projection images themselves, without consideration of any slip models. We performed a series of back-projection runs for narrow, overlapping passbands having center frequencies of 0.125, 0.25, 0.50, 1.0, and 2.0 Hz, with the upper corner defined as 1.414 times the center value and lower corner defined as 0.707 times the center value. Four-pole Butterworth filters were used, and the corresponding filter responses are shown in Figure 11. Collectively, they span the spectral band over which back-projection imaging

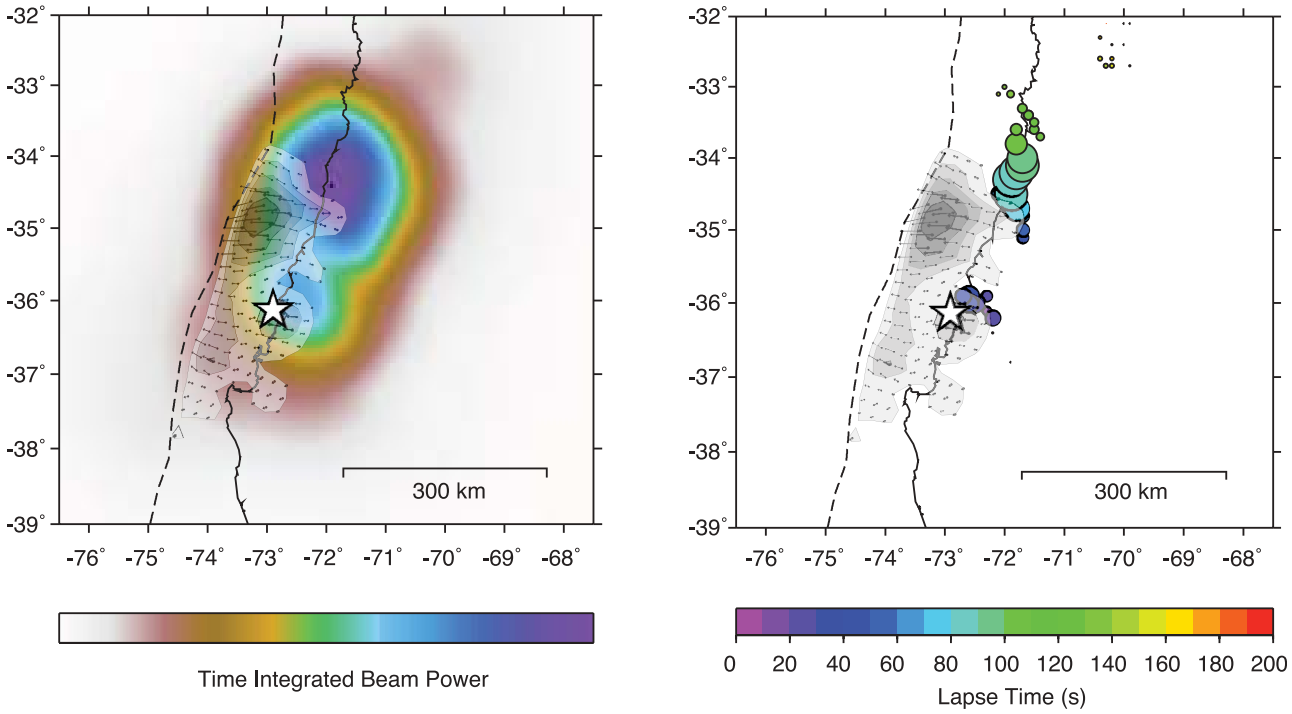

Figure 9. Comparison of our preferred model of cumulative slip (derived with Vr = 2.0 km/s to match teleseismic, geodetic, and tsunami data) and results for *P* waves back projected from the dense North America configuration of seismometers (Figure 1). The colored circles represent locations of beam power local maxima, with circle size proportional to beam power. There is a clear spatial difference in the location of peak slip and peak short-period radiation.

of earthquake ruptures with teleseismic body wave data is generally viable. Processing was similar to that described above except for the following accommodations related to the variable dominant period: the sliding window length was set at three times the dominant period (e.g., 24 s for longest-period band, 12 s for the next longest, and so on) and the frame averaging was set at approximately seven times the dominant period (e.g., 56 s for the longest period, 28 for the next longest, and so on).

[43] Back-projection results from the five runs are presented in Figure 11. Each was carried out with fourth-root stacking using the data from the dense North American geometry (Figures 1a and 1b). For lapse times less than 30 s, there is little difference among the passbands; however, at longer times into the rupture (~>60 s) the lowest-frequency images systematically image energy to the west and updip of the higher-frequency energy, as well as being more to the south. Interestingly, there is little difference between the results constructed with center frequencies of 0.25 Hz and higher, other than what is expected from the varying resolution. In other words, there is no smooth eastward drift of beam power as the center frequency is gradually increased, rather there seems to be an abrupt shift across a threshold value somewhere in the range of 0.125–0.25 Hz.

7. Robustness Test Based on Aftershock Locations

[44] While the diverse network configurations considered here intrinsically differ in their constraint on short-period

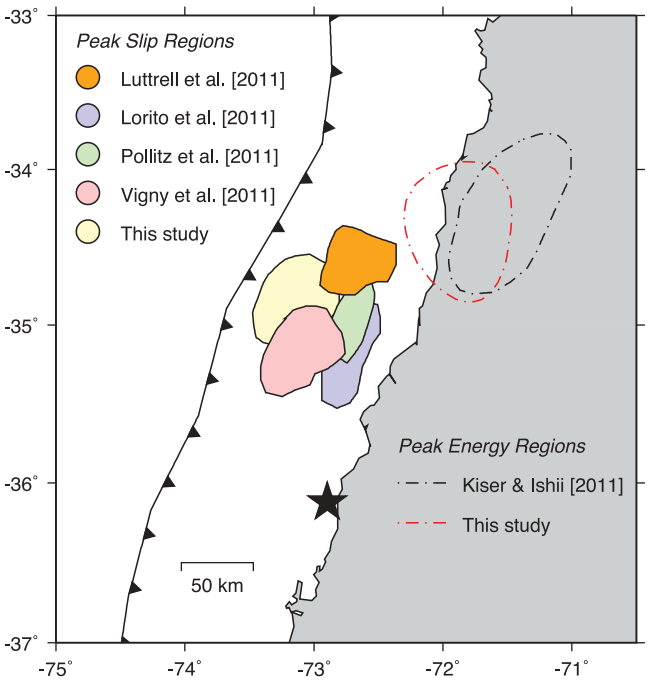

Figure 10. Comparison of regions of peak, short-period, time-integrated beam power from this study and that of *Kiser and Ishii* [2011], with regions of peak slip from five independent finite fault models. The black star is the National Earthquake Information Center epicenter, and the serrated line is the Peru-Chile trench.

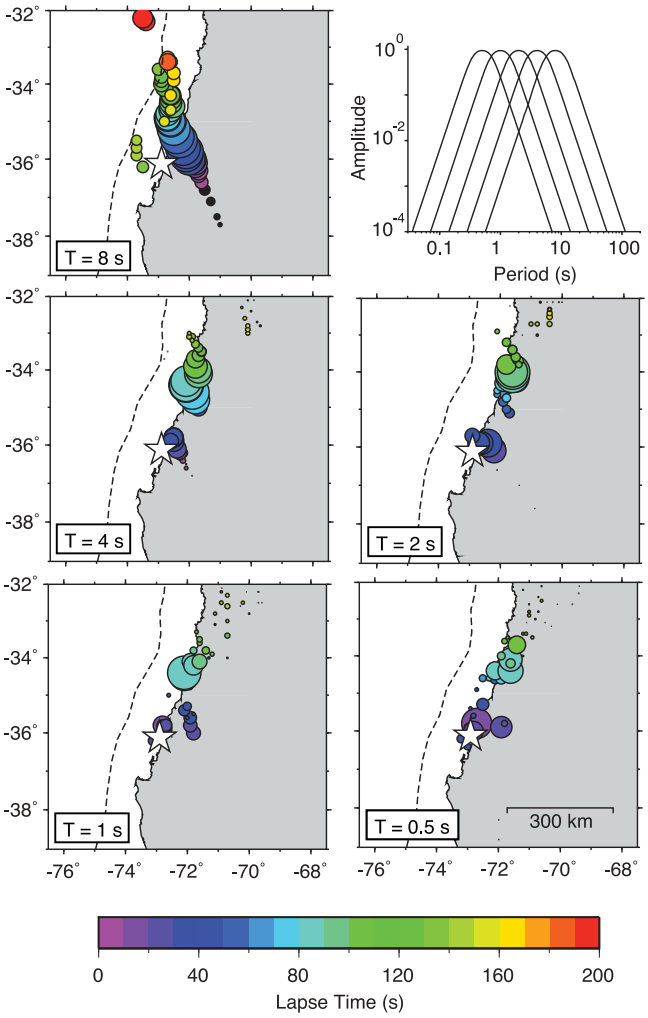

Figure 11. Back-projection results using the dense North American configuration of seismometers in five narrow, overlapping passbands. The amplitude responses of the filters are shown in the top right, and peak maxima for the bands centered at 0.5, 1, 2, 4, and 8 s are shown in the other panels. Circle size is proportional to beam power and time is indicated by the color. The longest-period band shows distinctly different results than the five other bands, with energy concentrated to the south and west (updip) of the four other bands. An animation of these back projections is provided in the auxiliary material.

imaging of the source region, they are consistent in placing primary short-period sources in the same region (Figures 1–4). We do not believe this is the result of bias in the propagation models because three of the networks are at different azimuths, however, we consider an independent check. To determine if our back-projection imaging is subject to a systematic location bias that artificially mislocates loci of short-period sources in the downdip direction, we experimented with back projection of *P* waves from 55 aftershocks within the first 3 h after the main shock with magnitude of at least 5.0 m_b located by the USGS. We used the same station corrections determined from the MCCC analysis of the main shock *P* waves. The aftershocks were small enough to be considered point sources, and beam power concentrations in the back-projection images can be considered epicentral estimates. If the back projection derived epicenters are systematically different than the USGS epicenters, it could imply that the locations of short-period energy release during main shock are also biased.

[45] The most favorable array geometry for imaging the Chile rupture was for *P* waves recorded in North America, and here we used the sparse version of this array (Figures 1e and 1f) since it provides results very similar to the dense version (Figures 1a and 1b) but is less computationally intensive. In Figure 12 we present representative results of imaging the *P* signal time intervals of the data for 10 aftershocks. There is a tendency for the back-projection locations to be displaced 10–30 km to the northeast of the corresponding USGS locations, however this is too small to explain our observations of spatial variation of the main shock spectral radiation. In the various comparisons of back-projection images with finite fault models that we have explored, the major high-frequency energy source in the north is always found 50–100 km east of the large slip concentration constrained from modeling longer-period seismic data and geodetic data.

8. Discussion

[46] Imaging the rupture of the 2010 Chile earthquake by back projecting teleseismic body waves is challenging because only a single cluster of seismometers (in North America) exists at the preferred distance range of 30°–95° for which direct *P* waves turn in the relatively homogeneous lower mantle. For other recent large events that have been successfully imaged via back projection (i.e., Sumatra 2004,

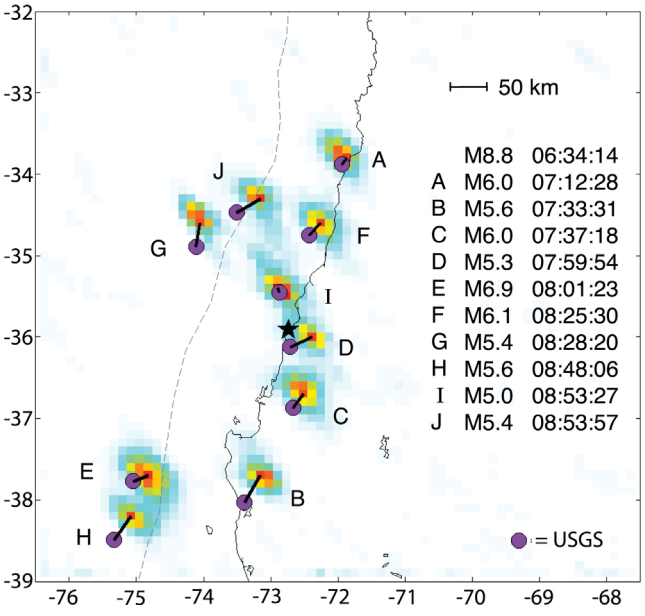

Figure 12. Comparison of back projection derived locations for 10 aftershocks with the epicenters reported by the USGS. There is only a very slight systematic offset to the northeast, implying that the differences in the rupture models shown in Figure 9 are not the result of a processing artifact but instead reflect an actual difference in the radiation of short- and long-period energy.

Wenchuan 2008, and Japan 2011), at least two distinct regional configurations of seismometers were available in the preferred distance range. This is important because the distribution of coherent short-period energy imaged in the source region can vary depending on the portion of the focal sphere that is sampled by the regional array. Comparing and/or combining multiple independent images of the rupture can thus help in identifying the robust features of the earthquake source. Direct combination of images formed from data at different azimuths is generally hard to justify given the variability in source illumination and the level of imaging artifacts that we have observed, but it may be useful in some cases.

[47] A second complicating factor is that the North American network is located along the general strike direction of the shallow-dipping Chile subduction zone, and many of the *P* waves were emitted in near-nodal radiation pattern directions. Especially for the short periods used in our back-projection analyses, this tends to increase the complexity of the waveforms and decrease the coherence. In addition, the southerly expansion of the Chile rupture indicated by aftershock locations and finite-fault models is toward azimuths away from the North American network and thus more poorly resolved by back projection using stations to the north. This is in part due to the swimming artifact associated with a space-time trade-off when locating out-of-network seismic sources. The natural smearing of back-projected energy toward the receiver array in space and time has the potential to disrupt or partially cancel energy associated with a source moving in the opposite direction. In addition, directivity effects on short-period energy released at the rupture front will favor coherent energetic arrivals being observed at azimuths in the direction of rupture, not opposite to the direction of rupture.

[48] We experimented with back-projection imaging from three additional station configurations, two of which yielded results consistent with those found for the North American geometry. Although the formal resolution of the configurations in Japan and Europe is lower than for the North American array, short-period radiation animations (see auxiliary material) derived from *PKIKP* waves recorded in Japan and *PP* waves recorded in Eurasia do share some general space-time features seen in the North American *P* wave back projections. In particular, the *PP* and *PKIKP* back projections both showed evidence for a strong short-period energy release about 150–250 km to the northeast of the epicenter near the coast, about 75–85 s after the origin time. The *PP* images also show significant energy for a southern short-period wave source consistent with bilateral faulting inferred from finite fault models, but only weakly visible in back-projection images derived from the North America *P* waves and the Japan *PKIKP* waves.

[49] An azimuthally extensive configuration that we considered provided poorer results. Back-projection images from relatively low frequency direct *P* waves recorded at a globally distributed array of 42 stations emphasized near-epicentral energy that was released within the first 20–30 s of the rupture, and provided little resolution of the ensuing bilateral rupture. We confirmed that this geometry had relatively poor ability to image the Chile rupture by back projecting synthetic *P* waves calculated for a finite fault model. The resulting images showed a poor correspondence to the input slip distribution, primarily because of the lack of coherence among *P* waves that so diversely sampled the focal sphere. For shallow dipping fault planes like the Chile event, teleseismic *P* wave trains vary significantly as a function of azimuth and generate incoherent waves that do not constructively interfere. It is possible that back projecting the envelopes of the globally recorded *P* waves would do a better job of locating the moving rupture, however it would be at much lower resolution than using a phased array approach. The relative success of a global array configuration in rupture imaging of the 2008 Wenchuan earthquake is probably owing to the steeper dip of the fault plane, leading to a more homogeneous sampling of the focal sphere, and higher coherence of the *P* wave trains, along with occurrence of localized impulsive subevents within the rupture. We believe that back projection of signals with periods longer than 5 s, as done for this configuration, is usually of marginal value, and procedures that correct for the Green's functions, as in point source or finite fault inversions, are preferable for evaluating the longer-period rupture process.

[50] The accuracy of rupture images derived with the primary North American configuration of direct *P* waves was further investigated by back projecting synthetics for a suite of finite fault models derived with constant rupture velocities that varied from 1.5 to 3.0 km/s in steps of 0.25 km/s. The corresponding images showed a high degree of similarity with input slip distributions, tracking the overall length of the rupture zone as it evolved from about 400 km to 800 km as the assumed rupture velocity increased. The overall width of the rupture zone was also recovered reasonably well. As expected, the location of the stronger northern asperity was in general better recovered than that of the southern asperity.

[51] Our synthetic back projections indicated that the longitudinal resolution of the northern asperity was fairly good with the North American geometry. If the short-period radiation matched the slip distribution shown in our FFM inferred from longer periods, then the back projections should have been able to resolve it. Therefore, there is a discrepancy for the location of seismic radiation from the northern portion of the rupture as a function of frequency, with the short-period energy being radiated from a more downdip location than the longer-period energy. We found a similar phenomenon when back projecting energy to the dense North American geometry in a series of narrow, systematically increasing frequency bands. More recent FFMs that we have obtained move the northern strong slip patch slightly downdip of our earlier solution, but not far enough to coincide with the back-projection results. We also note that a recent independent back-projection study of the Chile earthquake [*Kiser and Ishii*, 2011] found similar locations for the short-period energy, and if anything it was located even further downdip, with all the beam power maxima clearly imaging beneath land.

9. Conclusions

[52] The evidence presented here supports an interpretation of the teleseismic short-period seismic energy from the great 2010 Chile earthquake originating from the downdip portion of the megathrust along or eastward of the Chilean coastline, with relatively high rupture velocity (2.5–3.0 km/s) expanding along strike at least to 34°S and possibly as far

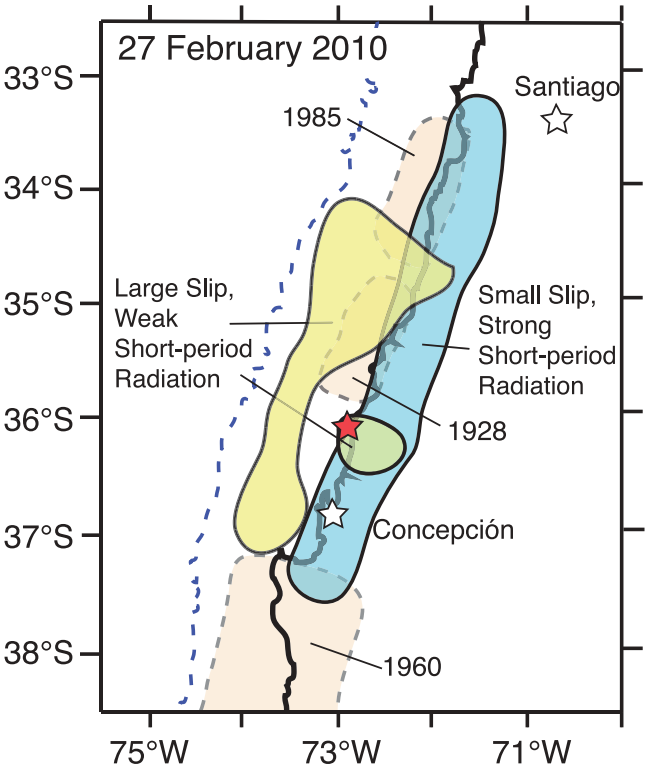

Figure 13. Schematic summary illustration indicating the locations of strong, coherent short-period energy release (blue area) and regions of large slip (yellow areas) for the great Chile earthquake of 2010. The red star indicates the event epicenter from the USGS (PDE-W). Approximate slip regions of large earthquakes in 1928, 1985, and 1960 are indicated. The trench is indicated by a blue dashed line, and the coastline of Chile is indicated by a solid black line.

north as 33.5°S. The long-period seismic radiation appears to have mainly occurred updip of this region, with relatively little short-period radiation from the vicinity of strong slip patches, and more to the south (peak slip near 35°S) with an effective fault area expansion rate closer to 1.75–2.0 km/s. It is possible that there was weak short-period radiation from a more rapidly expanding rupture front at shallow depth, with slow risetime and long slip duration, but this is hard to resolve teleseismically and still implies an effective decoupling of the short-period seismic radiation from the primary slip, as shown schematically in Figure 13.

[53] This is even more convincingly observed for the 11 March 2011 Tohoku (M_w 9.0) earthquake [*Koper et al.*, 2011], and it appears to also be the case for the 26 December 2004 Sumatra (M_w 9.2) earthquake. The implications are very important for the interpretation of short-period back projections of signals from great earthquakes; while interesting and important aspects of the rupture process can be revealed, it is not at all clear that variability of short-period radiation should be associated with strong slip variations of the faulting and vice versa. In addition, use of back projections to define rupture velocity for a priori imposition on finite fault models [e.g., *Lay et al.*, 2010] may bias slip distributions by allowing too fast of rupture expansion.

[54] **Acknowledgments.** This work made use of GMT and SAC software. The IRIS, F-net, and Orfeus data centers were used to access the seismic data. This work was supported by NSF grants EAR0635570 (T.L.), EAR098660 (T.L.), and EAR0951558 (K.D.K.). We thank H. Kanamori for discussions about strengths and weaknesses of back-projection approaches. We also thank an anonymous referee, Frank Krüger, and Associate Editor P. Martin Mai for providing thoughtful reviews.

References

Comte, D., A. Eisenberg, E. Lorca, M. Pardo, L. Ponce, R. Saragoni, S. K. Singh, and G. Suárez (1986), The 1985 central Chile earthquake: A repeat of previous great earthquakes in the region?, *Science*, *233*, 449–453, doi:10.1126/science.233.4762.449.

Delouis, B., J.-M. Nocquet, and M. Vallée (2010), Slip distribution of the February 27, 2010 M_w = 8.8 Maule earthquake, central Chile, from static and high-rate GPS, InSAR, and broadband teleseismic data, *Geophys. Res. Lett.*, *37*, L17305, doi:10.1029/2010GL043899.

Farías, M., G. Vargas, A. Tassara, S. Carretier, S. Baize, D. Melnick, and K. Bataille (2010), Land-level changes produced by the M_w 8.8 2010 Chilean earthquake, *Science*, *329*, 916, doi:10.1126/science.1192094.

Hayes, G. P., P. S. Earle, D. J. Wald, H. Benz, C. Ji, and G. Shao (2010), Real time teleseismic source inversion of the Maule earthquake, Abstract G31B-01 presented at 2010 Fall Meeting, AGU, San Francisco, Calif., 13–17 Dec.

Ishii, M., P. M. Shearer, H. Houston, and J. E. Vidale (2005), Extent, duration and speed of the 2004 Sumatra-Andaman earthquake imaged by the Hi-net array, *Nature*, *435*, 933–936.

Kanasewich, E. R., C. D. Hemmings, and T. Aplaslan (1973), Nth-root stack nonlinear multichannel filter, *Geophysics*, *38*, 327–338, doi:10.1190/1.1440343.

Kennett, B. L. N., E. R. Engdahl, and R. Buland (1995), Constraints on seismic velocities in the Earth from travel times, *Geophys. J. Int.*, *122*, 108–124, doi:10.1111/j.1365-246X.1995.tb03540.x.

Kiser, E., and M. Ishii (2011), The 2010 M_w 8.8 Chile earthquake: Triggering on multiple segments and frequency-dependent rupture behavior, *Geophys. Res. Lett.*, *38*, L07301, doi:10.1029/2011GL047140.

Koper, K. D., A. R. Hutko, T. Lay, C. J. Ammon, and H. Kanamori (2011), Frequency-dependent rupture process of the 11 March 2011 M_w 9.0 Tohoku earthquake: Comparison of short-period *P* wave back-projection images and broadband seismic rupture models, *Earth Planets Space*, *63*, 599–602, doi:10.5047/eps.2011.05.026.

Krüger, F., and M. Ohrnberger (2005), Tracking the rupture of the M_w 9.3 Sumatra earthquake over 1,150 km at teleseismic distance, *Nature*, *435*, 937–939.

Lay, T., C. J. Ammon, H. Kanamori, K. D. Koper, O. Sufri, and A. R. Hutko (2010), Teleseismic inversion for rupture process of the 27 February 2010 Chile (M_w 8.8) earthquake, *Geophys. Res. Lett.*, *37*, L13301, doi:10.1029/2010GL043379.

Lorito, S., F. Romano, S. Atzori, X. Tong, A. Avallone, J. McCloskey, E. Boschi, and A. Piatanesi (2011), Limited overlap between the seismic gap and coseismic slip of the great 2010 Chile earthquake, *Nat. Geosci.*, *4*, 173–177, doi:10.1038/ngeo1073.

Luttrell, K., X. Tong, D. Sandwell, B. Brooks, and M. Bevis (2011), Estimates of stress drop and crustal tectonic stress from the 27 February 2010 Maule, Chile, earthquake: Implications for fault strength, *J. Geophys. Res.*, *116*, B11401, doi:10.1029/2011JB008509.

McFadden, P. L., B. J. Drummond, and S. Kravis (1986), The Nth root stack: Theory, applications, and examples, *Geophysics*, *51*, 1879–1892, doi:10.1190/1.1442045.

Muirhead, K. J., and R. Datt (1976), The N-th root process applied to seismic array data, *Geophys. J. R. Astron. Soc.*, *57*, 197–210.

Okal, E., S. Hongsresawat, and S. A. Stein (2010), Normal modes excited by the 2010 Chile earthquake; no evidence for an ultra-slow component to the source, Abstract U21B-06 presented at 2010 Fall Meeting, AGU, San Francisco, Calif., 13–17 Dec.

Pollitz, F. F., et al. (2011), Coseismic slip distribution of the February 27, 2010 *Mw* 8.8 Maule, Chile earthquake, *Geophys. Res. Lett.*, *38*, L09309, doi:10.1029/2011GL047065.

Rost, S., and C. Thomas (2002), Array seismology: Methods and applications, *Rev. Geophys.*, *40*(3), 1008, doi:10.1029/2000RG000100.

Satake, K., and Y. Fujii (2010), Seismic moment and slip distribution of the 1960 and 2010 Chilean earthquakes as inferred from tsunami waveforms, Abstract G31B-02 presented at 2010 Fall Meeting, AGU, San Francisco, Calif., 13–17 Dec.

Tanimoto, T., and C. Ji (2010), Afterslip of the 2010 Chilean earthquake, *Geophys. Res. Lett.*, *37*, L22312, doi:10.1029/2010GL045244.

Tong, X., et al. (2010), The 2010 Maule, Chile earthquake: Downdip rupture limit revealed by space geodesy, *Geophys. Res. Lett.*, *37*, L24311, doi:10.1029/2010GL045805.

VanDecar, J. C., and R. S. Crosson (1990), Determination of teleseismic relative phase arrival times using multi-channel cross-correlation and least squares, *Bull. Seismol. Soc. Am.*, *80*, 150–169.

Vigny, C., et al. (2011), The 2010 M_w 8.8 Maule mega-thrust earthquake of central Chile, monitored by GPS, *Science*, *332*, 1417–1421, doi:10.1126/science.1204132.

Wessel, P. W., and W. H. F. Smith (1991), Free software helps map and display data, *Eos Trans. AGU*, *72*, 441, 445–446, doi:10.1029/90EO00319.

Xu, Y., K. D. Koper, O. Sufri, L. Zhu, and A. R. Hutko (2009), Rupture imaging of the M_W 7.9 12 May 2008 Wenchuan earthquake from back projection of teleseismic *P* waves, *Geochem. Geophys. Geosyst.*, *10*, Q04006, doi:10.1029/2008GC002335.

Yamazaki, Y., and K. F. Cheung (2011), Shelf resonance and impact of near-field tsunami generated by the 2010 Chile earthquake, *Geophys. Res. Lett.*, *38*, L12605, doi:10.1029/2011GL047508.

A. R. Hutko, Data Management Center, Incorporated Research Institutions for Seismology, 1408 NE 45 St., Ste. 201, Seattle, WA 98105, USA. (alex@iris.washington.edu)

K. D. Koper and O. Sufri, Department of Geology and Geophysics, University of Utah, Salt Lake City, UT 84112, USA. (koper@seis.utah.edu; oner.sufri@gmail.com)

T. Lay, Department of Earth and Planetary Sciences, University of California, Santa Cruz, CA 95064, USA. (tlay@ucsc.edu)